Energy Storage Materials 65 (2024) 103093

Contents lists available at ScienceDirect

Energy Storage Materials

journal homepage: www.elsevier.com/locate/ensm

# Cobalt atom-cluster interactions synergistically enhance the activity of oxygen reduction reaction in seawater

Junda Lu [a,#], Qi Lu [b,#], Yue Guo [a], Xiangqi Chen [a], Zexiang Yin [a], Yanhui Cao [b], Yuanyuan Guo [a], Jinfeng Zhang [b], Haozhi Wang [a,*], Yang Wang [a], Xuerong Zheng [a,b,*], Kenneth I. Ozoemena [c], Yida Deng [a,b,*]

[a] School of Materials Science and Engineering, Key Laboratory of Pico Electron Microscopy of Hainan Province, Hainan University, Haikou, Hainan Province 570228, P R China

[b] School of Materials Science and Engineering, Key Laboratory of Advanced Ceramics and Machining Technology of Ministry of Education, Tianjin University, Tianjin 300072, P R China

[c] Molecular Sciences Institute, School of Chemistry, University of the Witwatersrand, Johannesburg 2050, South Africa

ARTICLE INFO

*Keywords:*
High temperature shock
Atomic clusters
Chlorine pre-absorption
oxidation–reduction reaction
Seawater battery

ABSTRACT

Seawater electrocatalysis is highly desired for a variety of energy storage and conversion systems, such as water splitting and metal fuel cells that directly using seawater as electrolyte. However, the adsorption of chloride ions ($Cl^-$) on active sites of cathodes would worsen the oxygen reduction reaction (ORR) activity and stability, thus lowering the battery performance. In this work, we firstly designed an electrocatalyst model, in which the Co atomic clusters were closely surrounded by satellite Co single atoms on N-doped carbon substrates, designated as Co-ACSAs. The theoretical calculation results suggested that the Co clusters possess stronger $Cl^-$ binding energy and acted as pre-adsorption group for $Cl^-$, thus fully exposed Co single atoms as ORR active sites with stronger $O_2$ adsorption energy to promote the oxygen reduction reaction process. Then, we developed an ultrafast high temperature shock strategy to synthesize the Co-ACSAs by controlling the N concentration in carbon substrates. Benefiting from the moderate interacting distance between Co clusters and satellite Co single atoms in Co-ACSAs, the electronic structure of Co clusters and Co single atoms was optimized through the modulation of the interconnected hexatomic ring. As a result, Co-ACSAs exhibit superior ORR activity and durability with on-set and half-wave potentials of 0.885 V and 0.782 V, respectively, and continuously catalyzing for 485 h in seawater electrolyte. The Co-ACSAs-based seawater battery exhibits a discharge voltage of 1.41 V at 5 mA $cm^{-2}$ and realized stable energy supply for more than 390 h.

## 1. Introduction

Harvesting energy from natural resources is of significant interest. Seawater is the most abundant natural resource, covering 70 % of the Earth's surface [1–3]. Seawater electrocatalytic technologies, such as overall water splitting and metal fuel cells, provide great potential for directly converting seawater into hydrogen and electricity for powering the equipments that working on the sea [4–9]. Currently, the majority of seawater usage techniques are electrochemical devices, in which the oxygen reduction reaction (ORR) activity and stability of cathode electrocatalysts stand at the core for determining the overall performance of the energy storage and conversion battery systems [10–13]. However, differentiating from the battery in traditional alkaline electrolyte, the presence of chloride ions ($Cl^-$) in seawater could heavily lower the ORR activity and durability of cathode electrocatalysts [1,14-18]. The adsorption of $Cl^-$ on the surface catalytic sites of electrocatalysts would poison the active sites, thus suppressing the adsorption of oxygen molecules, hampering the breakage of O—O bonds, and inducing the ORR pathway transfer from four-electron to two-electron [19–21]. Therefore, under the harsh seawater environment, the electrocatalysts need to satisfy the following requirements: (i) the catalytic active sites should have no interaction or low adsorption energy with $Cl^-$; (ii) the catalysts should have large active sites exposure to increase their contact with active species, such as protons, electrons, and oxygen intermediates; (iii)

* Corresponding authors.
*E-mail addresses:* hzwang001@hainanu.edu.cn (H. Wang), xrzh@hainanu.edu.cn (X. Zheng), yd_deng@hainanu.edu.cn (Y. Deng).
# These authors contributed equally: Junda Lu, Qi Lu.

https://doi.org/10.1016/j.ensm.2023.103093
Received 18 September 2023; Received in revised form 16 November 2023; Accepted 26 November 2023
Available online 27 November 2023

the active sites should possess optimal electronic and chemical bonding structure to promote the catalytic activity and stability.

Pt-based ORR electrocatalysts usually display high ORR efficiency. However, they are high cost and can be easily corroded in seawater electrolyte. Although the coating and defecting engineering strategies were developed, their stability still cannot reach the industrial requirement. Recently, single-atom (SAs) catalysts, mainly the metal-nitrogen-carbon (M-N-C) series, are highly efficient for the ORR process due to their highly atomic utilization, tunable electronic structure, superior intrinsic catalytic activity for each active site [22–27]. Moreover, the rational design of the single atomic electrocatalysts would endow them possess superior chlorine-poisoning resistance and make them promising for being applied in seawater electrolyte [1,28]. For instance, Fe-SAs anchoring on graphene/CNT substrates (Fe-N-G/CNT) were synthesized by the microwave heating method and displayed an ORR half-wave potential of 704 mV in seawater with a discharge voltage of 1.18 V at 10 mA $cm^{-2}$ in seawater metal-air batteries (SWBs) [29,46]. However, the activity and stability of SAs are trade-off relationships for the ORR process [13]. The common strategy to balance the activity and stability is to tune the electronic modulation between metallic sites and substrates by doping heteroatoms or constructing defects, but the regulation range is narrow and difficult to break the activity-stability trade-off relationship [30–34]. Moreover, due to the sparse distribution of metal atoms in SAs, the electronic interactions between these metal atoms are generally negligible [13,35,36]. The recently reported results show that further modulation of the electronic structure of single atoms by introducing neighboring atomic clusters (ACs) may provide an opportunity to enhance their intrinsic catalytic activity and stability [16, 37-39]. ACs could provide active sites with adjacent metal atoms while keeping them as individual sites. The potential synergistic interactions between ACs and SAs result in unique electronic properties and are promising for enhancing the electrocatalytic performance [40–42]. However, constructing stable ACs modulated SAs (ACSAs) on conductive substrates still remains a great challenge due to their high surface energy and easy for agglomeration into nanoparticles. In addition, little attention has been paid to studying the ORR mechanism of ACSAs in seawater electrolyte, which may provide a new way to design active and stable electrocatalysts for SWBs.

In this work, we designed atomic-level electrocatalysts in which the Co atomic clusters (Co-ACs) were surrounded by satellite Co single atoms (Co-SAs), and we designated the electrocatalysts as Co-ACSAs. Interestingly, the theoretical calculation results suggest that the Co-ACs in Co-ACSAs show stronger $Cl^-$ adsorption energy but lower $O_2$ adsorption energy. On the contrary, Co-SAs show lower $Cl^-$ adsorption energy but stronger $O_2$ adsorption energy. The calculation results indicate that the Co-ACs in Co-ACSAs would play a critical role in protecting Co-SAs from being poisoned by $Cl^-$, and the stronger $O_2$ adsorption energy on Co-SAs site would promote the ORR process in seawater electrolyte. Inspired by the primary theoretical calculations, we developed an ultrafast high temperature shock (HTS) strategy for anchoring Co-ACs and satellite Co-$N_4$ single atoms on N-doped carbon substrates (Co-ACSAs) in one step. The experimental and theoretical results suggest that benefiting from the optimal distance between Co-ACs and Co-SAs, the Co-ACs could modulate the electronic structure of nearby Co-SAs through the interconnected hexatomic ring, which can promote the adsorption of oxygen active species on Co-SAs and accelerate the formation of OOH* by reducing the corresponding energy barrier. The strong modulation between Co-ACs and Co-SAs in Co-ACSAs results in impressive ORR activity and long-term stability in seawater electrolyte, superior to the pure phase of Co-SAs and Co nanoparticles (Co-NPs). Using Co-ACSAs as cathode electrocatalysts, the as-assembled SWBs reached a peak power density of 96 mW $cm^{-2}$ and kept stable for at least 380 h for discharging at current density of 5 mA $cm^{-2}$ and the discharge voltage can reach 1.46 V in natural seawater, which achieved a new record in the area of seawater batteries.

## 2. Experimental

### 2.1. Material synthesis

$C_4H_6CoO_4{\cdot}4H_2O$ (Macklin, 99.5 %), urea (Macklin, 99 %), glucose (Macklin, 99 %), KOH (Macklin, 99 %), NaCl (Macklin, 99 %), Pt/C and Ni foam (Shanghai Hesen Electric Co., LTD, 20 wt%) were used as precursors without further purification.

Co-ACSAs were synthesized by the high temperature shock (HTS) technique. Cobalt (II) acetate tetrahydrate (44.26 mg), glucose (6 g) and urea (0.412 g) were dissolved in 5 mL ultrapure water at room temperature as precursor solution. Then, it was evenly coated on Ni foam (NF, 5 × 20 mm) and dried in the vacuum oven at 60 ℃ for 2 h. The coated NF was mounted on a glass slide substrate. Copper ribbons were employed as wires connected to the coated NF with external circuit. The silver paste was passed to both ends of the NF. The HTS shock treatment was performed by applying constant current (12 A) to NF in an argon-filled glove box for 7–8 s [43]. Similarly, 0.148 g and 0.72 g urea were added in the precursor solution in the precursor solution for preparing Co-NPs and Co-SAs, respectively. The N—C was prepared with the same synthetic process as described above, but no Cobalt (II) acetate tetrahydrate was added to the precursor solution.

### 2.2. Characterizations

The morphologies and micro-nanostructures were recorded using transmission electron microscopy (TEM, Thermo Scientific, Talos F200X G2) and high resolution TEM (HRTEM) equipped with energy dispersive spectroscopy (EDS). High-angle annular dark-field scanning transmission electron microscopy (HAADF-STEM) images were collected on the JEOL JEM-ARM200F. The elemental analysis was conducted on the inductively coupled plasma OES spectrometer (ICP-OES, SPECTROblue). Synchrotron X-ray absorption spectroscopy (XAS)measurements (Co K-edge XAS) were performed in transmission mode, using easy XAFS equipment. The Co foil and CoO were selected as the references for $Co^{0+}$ and $Co^{2+}$, respectively. The acquired EXAFS data were processed according to the standard procedures using the ATHENA module implemented in the IFEFFIT software packages [44]. To determine the valence states of the transition metals at different states of charge, we selected the nearly linear portion of the rising edge for integration and defined the integrated average intensity as the K-edge. Fortran-based HAMA code to do the Morlet wavelet transforms (MWT) of $k^2$ weighted EXAFS spectra [45]. For appropriate resolution in the R-and K-space, a wavelet parameter combination of $k = 15$ and $\sigma = 2$ was well suited to discriminate atomic contributions in the Fourier transforms of Co K-edge EXAFS spectra.

### 2.3. Electrochemical measurements

For preparing the slurry, 5 mg of the prepared catalyst was dispersed in a mixed solution of 40 μL Nafion (5 wt%) and 460 μL isopropanol alcohol and sonicated for 20 min. For catalyzing ORR, 4 μL of the slurry was dropped onto a polished glassy carbon electrode with the catalyst loading of 0.2 mg $cm^{-2}$ and was used as the working electrode. A graphite electrode was used as the counter electrode. Hg/HgO electrode was used in 0.1 M KOH and Ag/AgCl electrode was used in natural seawater and the mixture of 0.1 M KOH and 0.5 M NaCl as reference electrode, respectively. The reported potentials were transferred with reference to the reversible hydrogen electrode (RHE) according to the equation: $E_{vsRHE} = E_{vsHg/HgO} + 0.886$ V in 0.1 M KOH and $E_{vsRHE} = E_{vsAg/AgCl} + 0.689$ V in natural seawater and 0.1 M KOH + 0.5 M NaCl. For catalyzing ORR, the rotating disk electrode (RDE)was connected to an electrochemical workstation (CHI660E) and a controlled speed rotator (AFMSRCE, Pine Instruments). The ORR polarization curves for all catalysts were obtained at a scan rate of 5 mV $s^{-1}$ in natural seawater, 0.1 M KOH or 0.1 M KOH + 0.5 M NaCl with $O_2$ saturated. The ORR

linear sweep voltammetry (LSV) curves were acquired at disk rotation rates of 400, 800, 1200, 1600 and 2000 rpm for the RDE examination. The stability tests were investigated at room temperature in $O_2$-saturated natural seawater by continuous potential cycling between 0.05 and 0.9 V vs RHE at a scan rate of 50 mV $s^{-1}$ for 50,000 cycles. The initial and final LSV curves were collected for comparison. The chronoamperometry (CA) tests were performed at room temperature in $O_2$-saturated natural seawater by applying a potential of 0.6 V for 485 h. The number of electrons transferred (n) and kinetic current density ($J_k$) can be calculated from the Koutecky-Levich equation [29]:

$$\frac{1}{J}=\frac{1}{J_L}+\frac{1}{J_K}=\frac{1}{B\omega^{1/2}}+\frac{1}{J_K} \quad (1)$$

$$B=0.62nFC_0D_0^{2/3}V^{-1/6} \quad (2)$$

where J is the measured current density, $J_k$ and $J_L$ are the kinetic and limiting current densities, ω is the angular velocity of the disk, n is the number of electrons transferred in oxygen reduction, F is the Faraday constant (96,500 C $mol^{-1}$), $C_0$ is the bulk concentration of $O_2$ in KOH (with NaCl) ($1.2 * 10^{-6}$ mol $cm^{-3}$) and natural seawater ($0.25 *10^{-6}$ mol $cm^{-3}$), $D_0$ is the diffusion coefficient of $O_2$ in 0.1 M KOH ($1.9 *10^{-5}$ $cm^2$ $s^{-1}$) and natural seawater ($1.4 \times 10^{-5}$ $cm^2$ $s^{-1}$), and V is the kinematic viscosity of the electrolyte (0.1 M KOH: 0.01 $cm^2$ $s^{-1}$; natural seawater: 0.1 $cm^2$ $s^{-1}$).To evaluate the effective electrochemical active areas surface (ECSA) of the prepared samples, the electrochemical capacitance ($C_{dl}$) parameters were obtained from 1.02 to 1.07 V by CVs measurements at scanning rates of 3, 5, 10, 15, 20, 30, 40, 50, 60, 70, 80, 90 and 100 mV $s^{-1}$, respectively.

### 2.4. SWB assembly

The SWBs were assembled using an Mg alloy plate as an anode, natural seawater as electrolyte and as-prepared catalyst as cathode. 40 wt% Pt/C was used as a reference catalyst. The properties of all SWBs were evaluated under $O_2$-saturated conditions. To assess the electrochemical properties of flexible ZAB, the discharge curves and cycling stability measurements were tested under 1.0 mA $cm^{-2}$ and 5 mA $cm^{-2}$. The discharge performance, open circuit and cycling ability were carried out on a LAND-CT2001A testing device at room temperature.

### 2.5. DFT calculations

First principles calculations in the framework of density functional theory (DFT) were carried out based on the Cambridge Sequential Total Energy Package known as VASP [47]. The exchange–correlation functional under the generalized gradient approximation (GGA) [48] with norm-conserving pseudopotentials and Perdew–Burke–Ernzerhof functional was adopted to describe the electron–electron interaction [49]. An energy cutoff of 450 eV was used and a k-point sampling set of $2 \times 2 \times 1$ was tested to be converged. A force tolerance of 0.01 eV $Å^{-1}$, energy tolerance of $5.0 \times 10^{-7}$ eV per atom and maximum displacement of $5.0 \times 10^{-4}$ Å were considered. The vacuum space along the Z direction was set to be 15 Å, which was enough to avoid interaction between the two neighboring images. *OOH, *O and *OH groups were adsorbed on the active sites of the model. The Grimme method for DFT-D3 correction was used for all calculations [50]. The electrochemical model of ORR developed by Nørskov [51] can be divided into four one-electron reactions:

$$O_2 + * + (H_2O + e-) \rightarrow *OOH + OH^- \quad (3)$$

$$*OOH + e- \rightarrow *O + OH^- \quad (4)$$

$$*O + (H_2O + e-) \rightarrow *OH + OH^- \quad (5)$$

$$*OH + e- \rightarrow * + OH^- \quad (6)$$

Gibbs free energy changes can be calculated by the following four Eqs. (7)-(10):

$$\Delta G_1 = 4.92eV - \Delta G_{*OOH} \quad (7)$$

$$\Delta G_2 = \Delta G_{*OOH} - \Delta G_{*O} \quad (8)$$

$$\Delta G_3 = \Delta G_{*O} - \Delta G_{*OH} \quad (9)$$

$$\Delta G_4 = \Delta G_{*OH} \quad (10)$$

where the sum of ΔG1–4 is fixed to the negative of the experimental Gibbs free energy of formation of two water molecules ($-2\Delta_{H_2O}^{exp}$) = 4.92 eV. The over-potential of ORR is determined by the following equations:

$$\eta^{ORR} = 1.23 - U_{ORR} \quad (11)$$

$$U_{ORR} = -Max\,(\Delta G_{*OOH} - 4.92eV, \Delta G_{*O} - \Delta G_{*OOH}, \Delta G_{*OH} - \Delta G_{*O}, \Delta G_{*OH})/e \quad (12)$$

Free energy change ΔG of the reaction was calculated as the difference between the free energies of the initial and final states as shown below: [52]

$$\Delta G = \Delta E + \Delta ZPE - T\Delta S \quad (13)$$

where ΔE is the energy change between the reactant and product obtained from DFT calculations; ΔZPE is the change of zero-point energy; T equal to 300 K and ΔS denote temperature and change of entropy, respectively. $T = 300$ K was considered.

## 3. Results and discussion

### 3.1. The design principles and synthesis of catalysts using HTS

We firstly established an atomic electrocatalyst model in which the Co-ACs were closely surrounded by satellite Co-SAs in Co-ACSAs (Fig. 1a). The pure phase mode of Co-SAs on carbon substrates was also established for comparison. The density functional theory (DFT) calculations were performed to calculate the adsorption energies of $Cl^-$ and $O_2$ molecule on all potential catalytic sites, including the Co-AC and Co-SA sites in Co-ACSAs model, and as well as the isolated Co-$N_4$ site in pure phase of Co-SAs (Fig. 1b and Table S1). As shown in Fig. 1a, the Co-AC sites in Co-ACSAs show much stronger binding strength (−2.1696 eV) towards $Cl^-$ than that of Co-SA sites in Co-ACSAs (−0.9954 eV) and isolated Co-$N_4$ (−0.9144 eV). Meanwhile, the Co-SA sites in Co-ACSAs show stronger binding strength (3.5749 eV) towards $O_2$ molecule than that of Co-AC sites in Co-ACSAs (2.7496 eV) and isolated Co-$N_4$ (2.2794 eV). These results indicate that Co-AC would prefer to adsorb $Cl^-$ and thus making more Co-SA sites being exposed to the active oxygen species for ORR process. Briefly, the Co-AC may act as an umbrella for protecting the neighboring Co-SAs from being poisoned by $Cl^-$ in the seawater electrolyte. The synergistic effect between Co-AC and Co-SA sites in Co-ACSAs would simultaneously enhance the catalytic activity and stability of the catalysts towards ORR process. However, precisely synthesizing Co-ACSAs still face great challenge.

To put the theoretical results into practice, the HTS strategy was employed for the synthesis of Co-based electrocatalysts, and their particle dimensions were well controlled in a wide range from nanoparticles (NPs) to atomic clusters and further to single atoms, which were referred to as Co-NPs, Co-ACSAs, and Co-SAs. In the synthesis process, the mixture of cobalt acetate, glucose, and urea was coated onto the nickel foam (NF), and was fixed on the glass holder (Fig. S1). The EDS results show that no Ni can be observed in the catalysts, excluding the effect of Ni on the catalytic performance of catalysts (Fig. S2). The electric current of 12 A was applied on the heating setup in the Ar atmosphere and the sintering temperature can reach 1000 ℃ in milliseconds. The whole process can be finished in 8 s with ultrafast heating ($3 \times 10^3$ K $s^{-1}$) and cooling rate ($2 \times 10^3$ K $s^{-1}$) [43], which is far outpacing traditional

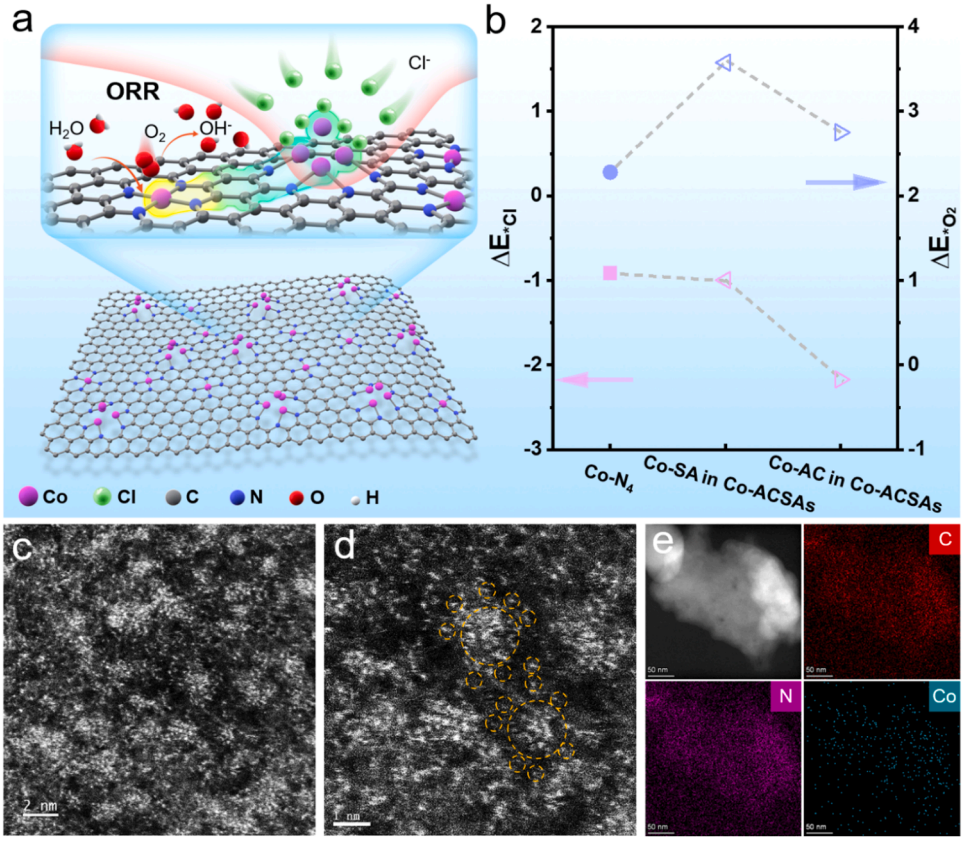


**Fig. 1.** (a) The schematic illustration of the proposed ORR catalytic mechanism of Co-ACSAs in seawater electrolyte. (b) The theoretical calculation results for the adsorption energy ($\Delta E_{ads}$) of $Cl^-$ and $O_2$ molecules towards different active sites in Co-ACSAs and Co single atoms. (c-d) The HAADF-STEM images and (e) elemental mapping images of Co-ACSAs.

chemical and physical processes (Fig. S1). During the heating process, the glucose and urea acted as C and N sources, respectively, and were transferred into N-doped carbon substrates (N—C) instantly (Fig. S3). As reported, the N sites in carbon substrates generally acted as the anchoring sites for stabilizing transition metal atoms (Fig. 1c). Thus, we controlled the mass ratio of N with the proportion of 1 wt%, 3 wt%, and 5 wt%, and then the Co atoms can be geometrically separated on the substrates and forming Co-NPs, Co-ACSAs, and Co-SAs, respectively. In addition, this synthetic method was developed into a universal strategy for synthesizing Fe-ACSAs and Ni-ACSAs (Fig. S4).

Transmission electron microscopy (TEM) and atomic-resolution high-angle annular dark-field scanning TEM (HAADF-STEM) were performed to investigate the microstructure and distribution of Co species in the N—C substrates. The TEM images show that the substrates of Co-ACSAs were layered structures (Fig. S5), which can expose more surface area to load atomic species and to improve the mass transfer rate during oxygen electrocatalysis. Moreover, no Co agglomerates are presented in Co-ACSAs, suggesting their well distribution on substrates. Brunauer-Emmett-Teller (BET) adsorption curves show that Co-ACSA has a largest specific surface area (794.2 $m^2\ g^{-1}$) than that of Co-NPs (503.6 $m^2\ g^{-1}$), and Co-SAs (612.5 $m^2\ g^{-1}$) (Fig. S6). The HAADF-STEM images (Fig. 1d-e) show that the atomic clusters were closely surrounded by the single atoms, and the distance between clusters and single atoms is smaller than 1.0 nm, which provides an excellent opportunity for the electronic modulation between the clusters and single atoms. The elemental mapping images show that the Co-ACSAs were uniformly distributed on the substrates (Fig. 1e). The Co-NPs and Co-SAs were also synthesized for comparison using the same strategy. As shown in the TEM images in Fig. S7–8, Co-SAs were evenly distributed on the N—C substrates and no clusters appeared in Co-SAs. The TEM and elemental mapping images of Co-NPs (Fig. S9–10) show that the Co nanoparticles with size of 3–5 nm were formed when the N proportion decreased to 1 wt%. The Co content in the three samples was measured by inductively coupled plasma optical emission spectrometer (ICP-OES), which are 4.36, 4.15 and 4.08 wt% for Co-NPs, Co-ACSAs and Co-SAs, respectively (Table S2). The above results suggest that the microstructure of Co species can be precisely regulated using the HTS strategy by tuning the N proportion in carbon support, which inspires us to explore their intrinsic physiochemical properties.

### 3.2. The structure analyses of the prepared catalysts

X-ray absorption spectroscopy (XAS) was performed to analyze the local electronic structure and the coordinated environmental variation of Co atoms in Co-ACSAs and Co-SAs. Fig. 2a shows the X-ray absorption near-edge structure spectra (XANES) of Co K-edge in Co-ACSAs, Co-SAs and reference samples (Co foil and CoO). To quantitatively evaluate the valence states of Co in the catalysts, we selected the nearly linear portion of the rising K-edge for integration and defined the integrated average intensity as the K-edge position [54–56]. The absorption threshold position of Co in Co-ACSAs and Co-SAs is close to that of CoO and far away from Co foil, implying the bivalent valence states of Co in the two catalysts. Subsequently, the valence states of Co in the catalysts were quantitatively calculated according to the K-edge position, which was $Co^{1.68+}$ and $Co^{1.73+}$ for Co-ACSAs and Co-SAs, respectively (Fig. 2b). The oxidation of Co in atomic level catalysts should be caused by the formation of Co-N-C ligands, in which the electrons were attracted from Co to N—C [42]. Comparing with that of Co-SAs, the lower valence state of Co in Co-ACSAs should be due to the existence of Co clusters, in which part of Co cannot hybridize with N—C substrates and thus forming Co-Co bonds in the clusters in Co-ACSAs. The $k^3$-weighted Fourier transforms of the extended X-ray absorption fine structure (FT-EXAFS)

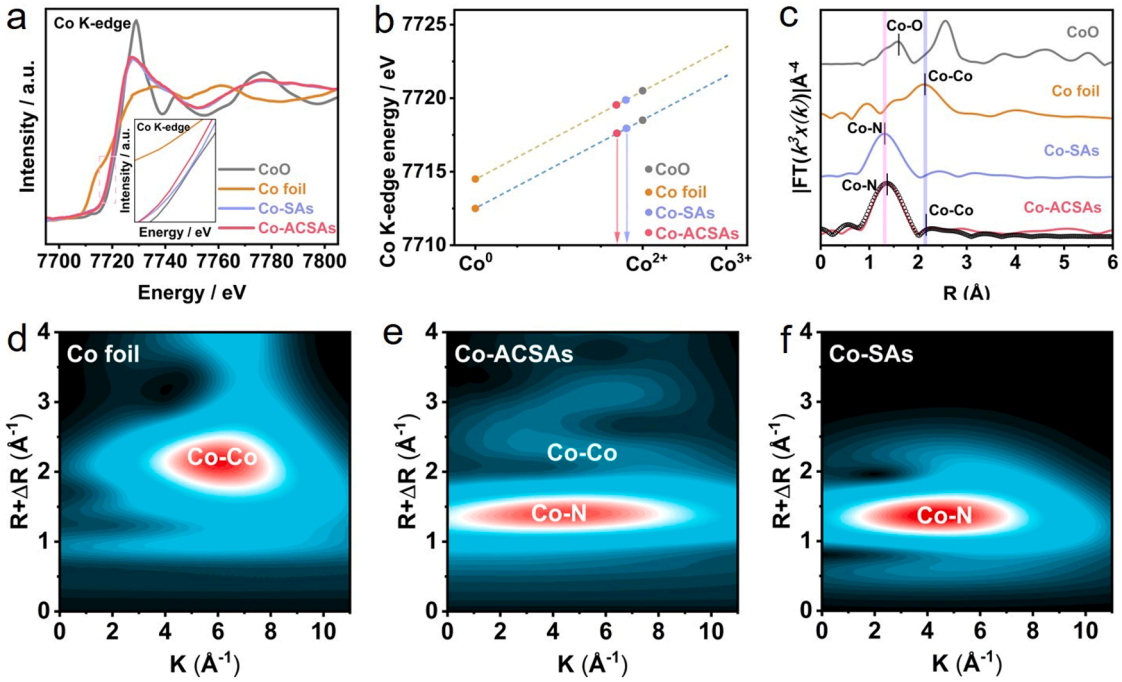


**Fig. 2.** (a) The XANES of Co K-edge for Co-ACSAs and Co-SAs with reference spectra of Co foil and CoO. (b) The calculated Co K-edge positions and valence states of Co in Co-ACSAs and Co-SAs. (c) FT spectra of $k^3$-weighted EXAFS spectra of Co K-edge in Co foil, Co-ACSAs and Co-SAs. (d-f) The MWT images of Co foil, Co-ACSAs and Co-SAs.

spectroscopy of Co-K-edge in Co-ACSAs and Co-SAs were shown in Fig. 2c. The Co-N peaks at around 1.4 Å in R space can be observed in both Co-ACSAs and Co-SAs. However, the Co-Co scattering peak at 2.2 Å was only observed in Co-ACSAs, demonstrating the co-existence of Co clusters and single atoms in Co-ACSAs [43,53]. The weak Co-Co scattering peak suggests that the particle size of Co clusters is very small and should be defined as an atomic cluster. Moreover, the Co K-edge EXAFS spectra Co-ACSAs was well fitted using backscattering paths of Co–N and Co-Co. As shown in Fig. S11 and Table S3, the coordination numbers of Co–N and Co-Co in Co-ACSAs are 2.54 and 1.92, respectively. The Morlet wavelet transforms (MWT) of EXAFS spectra is a powerful method to qualitatively identify and directly visualize the local bonding structure of metal atoms and identify the overlapping contributions that caused by the multiple-scattering phenomenon [57]. The MWT of $k^3$-weighted EXAFS spectra of Co in Co foil, Co-ACSAs and Co-SAs were shown in Fig. 2d-F. In Fig. 2d, the MWT contour plots show an intensity maximum at about 7.0 $Å^{-1}$ in k space, which can be assigned to the Co-Co scattering path in Co foil. Comparing to the MWT images of Co-SAs, both the Co-N and Co-Co maximas appeared in Co-ACSAs at 4.2 $Å^{-1}$ and 7.0 $Å^{-1}$ (Fig. 2e-F), respectively, which is consistent with the FT-EXAFS results.

### 3.3. Half-cell tests and the $Cl^-$-poisoning resistance analysis of active sites

Aiming at developing efficient and stable ORR electrocatalysts for the application in seawater batteries, the electrochemical properties of Co-ACSAs, Co-SAs and Co-NPs were systematically investigated in $O_2$-saturated natural seawater using a typical three-electrode system (Fig. 3). The natural seawater was obtained from the South China Sea (Fig. S12). All the Linear sweep voltammetry (LSV) curves were tested on the rotating disk electrode (RDE) by coating catalysts on glassy carbon electrodes with the rotation speed of 1600 rpm. The pure phase of N—C and commercial Pt/C were employed as counterparts. The LSV results (Fig. 3a) show that Co-ACSAs display impressive half-wave and on-set ORR overpotentials of $E_0 = 0.885$ V and $E_{1/2} = 0.782$ V (vs. RHE), which are much higher than that of Co-SAs (0.787 V and 0.701 V), Co-NPs (0.714 V and 0.608 V) and Pt/C (0.755 V and 0.632 V). The LSV curve of commercial Pt/C exhibits no obvious peak and limited current density, which may be caused by the serious poisonous $Cl^-$ in seawater. N—C shows weak ORR activity in natural seawater. Correspondingly, Co-ACSAs also has a smaller Tafel slope (125.73 mV $dec^{-1}$) than that of Co-SAs (158.12 mV $dec^{-1}$), Co-NPs (207.95 mV $dec^{-1}$), and Pt/C (289.84 mV $dec^{-1}$), indicating its superior ORR catalytic kinetics in natural seawater (Fig. 3b). Subsequently, the LSV curves were also evaluated on the electrodes without rotation, and the same ORR activity tendency was obtained (Fig. S13). Moreover, the electron transfer number (n) of Co-ACSAs, Co-SAs and Co-NPs were evaluated in natural seawater by testing the LSV curves at different rotation speeds. The fitted Koutecky–Levich (K-L) plots exhibit that the n values for Co-ACSAs, Co-SAs, and Co-NPs are 3.89, 3.15, and 2.48, respectively, suggesting that the Co-ACSAs possess the highest reaction kinetics with efficient four-electron pathway during the ORR process in natural seawater (Fig. 3c and Fig. S14). In addition, the Co-ACSAs shows remarkable ORR stability in natural seawater. After 485 h continuous chronoamperometric treatment, the Co-ACSAs displays the smallest degradation rate (8.57 %) at 0.65 V vs. RHE compared to Co-NPs (52.18 %) and Co-SAs (20.83 %) (Fig. 3d). The LSV curves of Co-ACSAs exhibits excellent stability with half-wave potential ($E_{1/2}$) loss of only 25 mV after 50,000 cyclic voltammetry (CV) cycles (Inset in Fig. 3d).

To further analyze the root reason for the ORR activity enhancement of Co-ACSAs comparing to that of Co-SAs and Co-NPs, the $Cl^-$ resistance behavior of the catalysts were analyzed in different electrolytes, such as KOH and the mixture of KOH + NaCl. As shown in Fig. 3e-f, the limit current density of Co-ACSAs has smaller degradation (1.2 mA $cm^{-2}$) when testing in the mixed $Cl^-$ containing electrolyte. However, Co-SAs and Co-NPs exhibit a tremendous decline (1.9 mA $cm^{-2}$) in the same condition, demonstrating more active sites in Co-SAs and Co-NPs were poisoned by $Cl^-$, but it has no obvious influence towards the active site exposure of Co-ACSAs. The ORR LSV curves for Co-ACSAs and Co-SAs were also tested in artificial seawater electrolyte with different NaCl concentrations. The results show that the ORR activity for Co-ACSAs displays no obvious change with the increase of NaCl concentration,

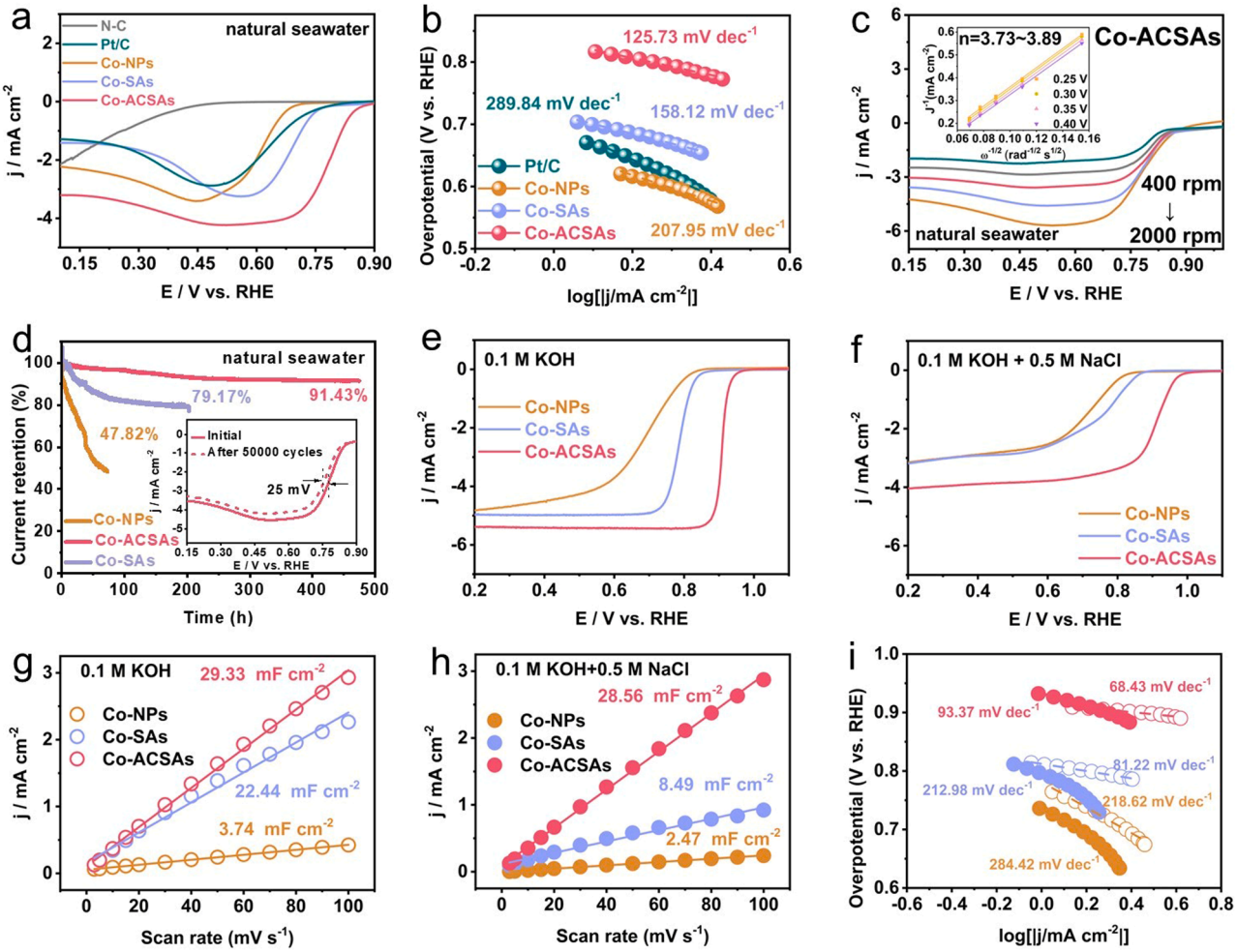


**Fig. 3.** (a) The ORR LSV polarization curves of Co-SAs, Co-ACSAs and Co-NPs at 5 mV $s^{-1}$ with a rotation speed of 1600 rpm in $O_2$-saturated natural seawater. (b) Tafel slopes. (c) ORR polarization curves of Co-ACSAs at different rotating speeds, inset shows fitted K–L plots of Co-ACSAs based on the LSV curves at 0.25, 0.30, 0.35, and 0.4 V. (d) Chronoamperometric curves of Co-NPs, Co-ACSAs and Co-SAs at 0.65 V vs RHE, inset shows ORR polarization curves of Co-ACSAs before and after 50,000 CV cycles. The ORR LSV polarization curves of Co-SAs, Co-ACSAs and Co-NPs at 5 mV $s^{-1}$ with a rotation speed of 1600 rpm in $O_2$-saturated (e) 0.1 M KOH and (f) 0.1 M KOH + 0.5 M NaCl. $C_{dl}$ values of the prepared Co-based catalysts in (g) 0.1 M KOH and (h) 0.1 M KOH + 0.5 M NaCl. (i) The corresponding tafel slopes.

demonstrating the synergistic effect between atomic clusters and single atoms in Co-ACSAs ensuring its remarkable Cl-corrosion resistance (Fig. S15). To further verify this hypothesis, the double-layer capacitance ($C_{dl}$) was performed to evaluate the effective electrochemical active surface area (ECSA) of the catalysts in the two kinds of electrolytes (Fig. 3g-h, Fig. S16 and Table S4) [58,59]. As shown in Fig. 3g-h, comparing to the tested results in KOH electrolyte, the ECSA values for Co-ACSAs that tested in $Cl^-$ containing electrolyte declined only 0.77 mF $cm^{-2}$ (2.6 % degradation), which is much smaller than that of Co-SAs (13.95 mF $cm^{-2}$, 62.2 % degradation) and Co-NPs (1.27 mF $cm^{-2}$, 33.9 % degradation). The above results suggest that the existence of $Cl^-$ would absorb on the surface of Co-SAs and Co-NPs and thus reduce the real active sites. The smaller variation of Tafel plot results for Co-ACSAs also confirmed its stronger $Cl^-$-poisoning resistance and superior ORR catalytic kinetics in $Cl^-$ containing electrolyte (Fig. 3i). The above results suggest that the co-existence of atomic clusters and single atoms in Co-ACSAs may play a strongly synergistic effect for improving the $Cl^-$-poisoning resistance and ensuring the Co active sites exposure, and thus enhancing the ORR catalytic activity in seawater electrolyte. The synergistic catalyzing mechanism for Co-ACSAs should be further unveiled with the assistance of the theoretical calculations.

### 3.4. Theoretical analyses

DFT calculations were performed to unveil the synergistic mechanism between atomic clusters and single atoms in Co-ACSAs for promoting the ORR activity in seawater electrolyte. The key factors, such as the geometrical size of atomic clusters and the distance between atomic clusters and single atoms, may have potential influence on the interaction between the two different Co species in Co-ACSAs, which were systematically investigated in the theoretical calculations. Firstly, two calculation models of Co atomic clusters ($Co_4$ and $Co_{13}$) were established (Fig. S17). The results show that the $Co_4$ in Co-ACSAs would display smaller Gibbs free energy (ΔG) barrier at the ORR rate-determine step (RDS) (Table S5–6). Therefore, we use $Co_4$ as the model of Co-AC and established $Co_4$/(Co-SA) as the model of Co-ACSAs for further calculation. We predict that the distance between Co-ACs and Co-SAs would potentially influence their electronic and bonding interaction, and thus the model with distance of 2.31 Å (no atom interval), 4.85 Å (two atoms interval), and 7.32 Å (one hexatomic ring interval) between Co-ACs and Co-SAs were established, as shown in Fig. 4a-d. For the model with distance of 2.31 Å, the Co-SAs would directly establish Co-Co ligands with Co-ACs ($Co_4$) and thus tend to form $Co_5$ clusters, resulting in much higher ΔG value of 0.7828 eV for the RDS. For the model with distance of 4.85 Å, strong electronic modulation would occur between Co-ACs

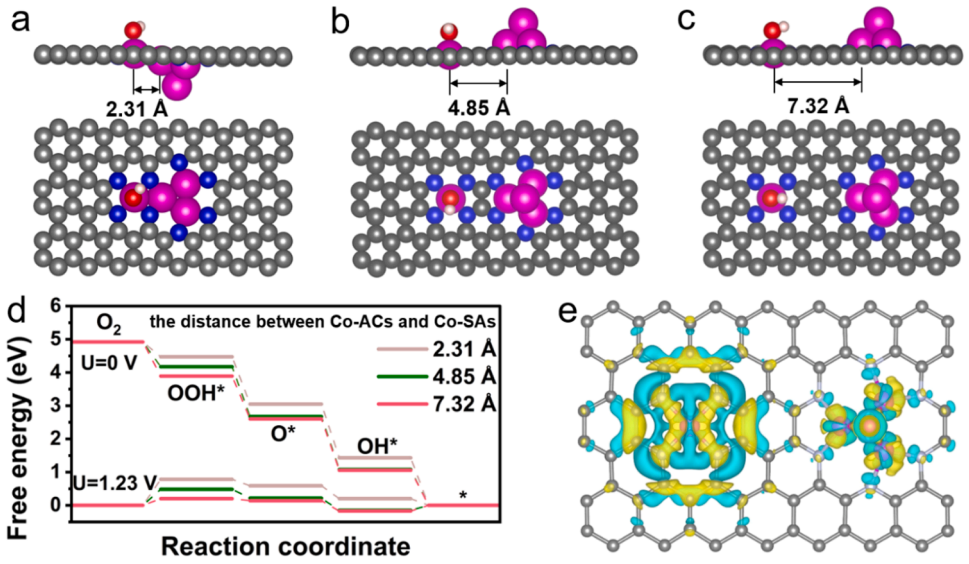


**Fig. 4.** Model structure of Co-ACSAs (Co: pink, N: blue and C: grey) with distance of (a) 2.31 Å, (b) 4.85 Å, and (c) 7.32 Å. (d) The calculated free energy diagrams for the ORR process of Co-ACSAs with different distance between clusters and single atoms. (e) The difference charge density of Co-ACSAs. (f) The $Cl^-$ and $O_2$ molecule adsorption energy ($Cl^-$: green, $O_2$: red) of Co-$N_4$ site and $Co_4$ site in the Co-ACSAs, and on pure phase of Co single atoms.

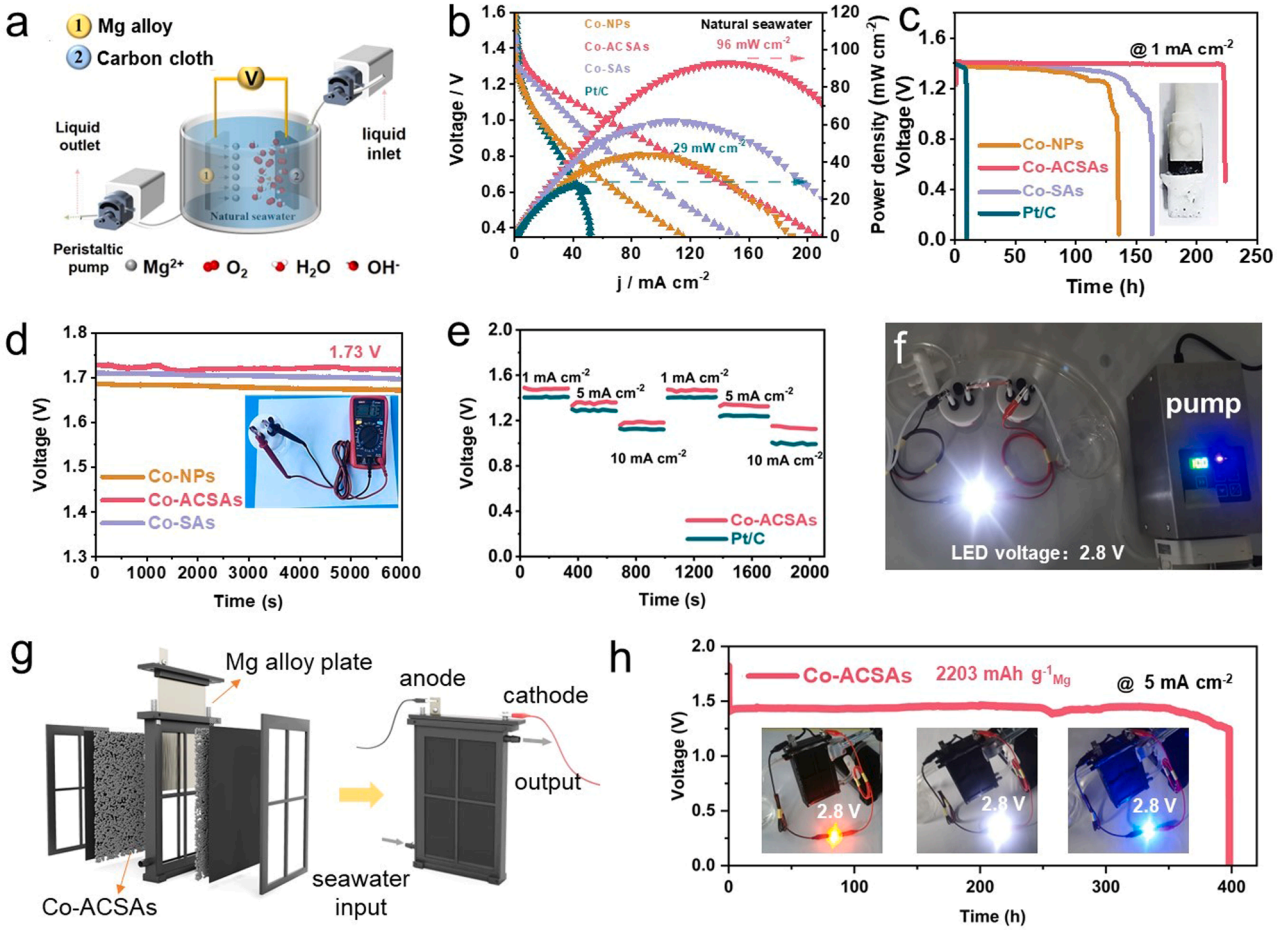


**Fig. 5.** (a) Schematic illustration of the SWB. (b) Discharge polarization curves and the calculated power density of the battery using Co-NPs, Co-ACSAs, Co-SAs and Pt/C as air electrodes. (c) Galvanostatic discharge curves of SWB catalyzed by Co-NPs, Co-ACSAs, Co-SAs and Pt/C at current densities of 1 mA $cm^{-2}$, insets are photographs of the cathode after the test. (d) Open-circuit plots of SWBs using Co-NPs, Co-ACSAs, and Co-SAs as air electrodes. (e) The discharge curves of the battery at different current densities using Co-ACSAs and Pt/C as air electrodes. (f) Digital photograph of LED lighted by two home-made Co-ACSAs based SWBs connected in series. (g) Schematic diagram of custom-made SWBs. (h) Discharge curves of Co-ACSAs based near-commercial SWB at current density of 5 mA $cm^{-2}$, insets are photographs of LED (2.8 V) lighted by two batteries connected in series.

and Co-SAs, resulting in serious electronic accumulation around active sites and larger energy barrier of 0.4829 eV for the determining step (Fig. 4b and Table S7–8). When increasing the distance between Co-ACs and Co-SAs to 7.32 Å, one hexatomic ring was located at the interval. Benefiting from the moderate electronic modulation between Co-ACs and Co-SAs through the hexatomic ring, both Co-ACs and Co-SAs have optimized electronic distribution density, which results in a smaller energy barrier of 0.1998 eV for the ORR determining step (Fig. 4c-e and Fig. S18). Then, the Co-ACSAs display a bigger downhill energy gap (−1.0301 eV) for the transformation of OO* to OOH* (Fig. 4d), thus promoting the whole ORR process under the optimal geometrical distance between Co-ACs and Co-SAs. The above calculation results demonstrate that Co-ACs would act as pre-adsorption sites towards $Cl^-$ and protect the adjacent Co single atoms from being poisoned by $Cl^-$, thus exposing Co single atoms as real catalytic sites for the ORR process.

### 3.5. Application of Co-ACSAs as cathodes in SWBs

The outstanding ORR catalytic performance of Co-ACSAs in seawater electrolyte encouraged us to explore its practical applications as the cathodes of SWBs. The home-made SWBs were assembled using Co-ACSAs as cathode, commercial Mg-alloy plate as anode, and natural seawater as the electrolyte. For comparison, Pt/C loaded on the carbon paper was employed as cathode. The schematic diagram of SWB is shown in Fig. 5a. In the test system (Fig. S19), the natural seawater was circulated with $O_2$-saturation during the test. The discharge polarization and corresponding power density curves were shown in Fig. 5b. The peak power density of SWB using Co-ACSAs as cathode reached 96 mW $cm^{-2}$, which is far outpacing that of Co-NPs (43 mW $cm^{-2}$), Co-SAs (62 mW $cm^{-2}$), commercial Pt/C (29 mW $cm^{-2}$) and the recently reported results (Table S10). Moreover, the galvanostatic discharge curves of SWBs at 1 mA $cm^{-2}$ show that Co-ACSAs can maintain the discharge voltage at 1.41 V for at least 240 h, which is much superior than that of Co-NPs, Co-SAs and Pt/C (Fig. 5c). In addition, the open circuit voltage of Co-ACSAs based SWB can reach 1.72 V and keep stable for at least 6000 s (Fig. 5d). The fitted Nyquist plots by the equivalent circuit model (Fig. S20 and Table S9) prove that Co-ACSAs has lower Rs and Rct values than the Co-NPs and Co-SAs, suggesting the fast electron transfer kinetics during ORR process.

The rate capability is an important factor for providing variable electricity to various of equipments in the deep and open sea. As shown in Fig. 5e, the Co-ACSAs based SWB can keep stable for providing variable current densities of 1, 5, and 10 mA $cm^{-2}$ with frequent variation. As we know, the discharging voltage, specific capacity and durability of Co-ACSAs based SWB reached a new record in the area of SWB (Table S10). To promote the SWB into practical application, two home-made SWBs were in series connected and can well power the light-emitting diodes (LED) for at least 24 h (Fig. 5f). Furthermore, we developed near-commercial SWB devices in which the area of air-electrodes reached 110 $cm^2$, and the sandwich-like packaging devices were developed by combining two air electrodes with one metallic electrode (Fig. 5g and S21). The as-assembled SWB devices can provide current density of 5 mA $cm^{-2}$ (1.45 V) and make the LED lights working stable for at least 390 h with a discharging capacity of 2203 mAh $g^{-1}_{Mg}$ (Fig. 5h). The efficient and stable application of custom-made devices provides extremely promising potential for the commercialization of Co-ACSAs based SWBs.

## 4. Conclusions

In summary, we developed an ultrafast method for synthesizing atomic Co-based electrocatalysts. The particle size of catalysts can be precisely controlled from nanoparticles to atomic clusters and further to single atoms by tuning the N mass ratio in carbon substrates. Comparing to that of Co-SAs and Co-NPs, Co-ACSAs exhibites superior ORR activity and durability in natural seawater. The experimental and theoretical calculation results suggest that the remarkable ORR performance of Co-ACSAs should be benefiting from the following factors: (1) The electronic modulation between single atoms and atomic clusters through the hexatomic ring in Co-ACSAs has optimized the electronic structure of Co-SAs and thus enhancing their intrinsic catalytic activity; (2) The stronger $Cl^-$ absorption energy of atomic clusters has protected single atoms from $Cl^-$ poisoning and thus ensured the large active sites exposure; (3) The independent existence between single atoms and clusters has synergistically enhanced the stability of Co-ACSAs. The Co-ACSAs based SWBs display outstanding prolonged discharge power density and stability and were primarily applied in large-scale devices for light illumination. The synergistic enhancement of Co-ACSAs in this study provides valuable guidance for the rational design of ORR electrocatalysts for developing energy conversion devices in seawater environments.

Supporting Information.

The experimental details, TEM and XAS; calculation of double-layer capacitance; DFT calculation results of Co-SAs, Co-ACSAs and Co-NPs, etc., are included in Supporting Information.

## CRediT authorship contribution statement

**Junda Lu:** Conceptualization, Data curation, Formal analysis, Writing – original draft, Writing – review & editing. **Qi Lu:** Methodology. **Yue Guo:** Methodology. **Xiangqi Chen:** Investigation, Visualization. **Zexiang Yin:** Software, Validation, Visualization. **Yanhui Cao:** Methodology. **Yuanyuan Guo:** Methodology. **Jinfeng Zhang:** Methodology. **Haozhi Wang:** Resources, Software. **Yang Wang:** . **Xuerong Zheng:** Funding acquisition, Project administration, Supervision. **Kenneth I. Ozoemena:** Data curation, Writing – review & editing. **Yida Deng:** Funding acquisition, Project administration, Supervision, Writing – original draft.

## Declaration of Competing Interest

The authors declare that they have no known competing financial interests or personal relationships that could have appeared to influence the work reported in this paper.

## Data availability

Data will be made available on request.

## Acknowledgments

This work was supported by the National Natural Science Foundation of China (52177220, 52231008, U23A20687) and International Science & Technology Cooperation Program of Hainan Province (GHYF2023007). The authors would also like to express gratitude to Dr. Jinfeng Zhang for her assistance in aberration-corrected HAADF-STEM characterizations at Tianjin University.

## Supplementary materials

Supplementary material associated with this article can be found, in the online version, at doi:10.1016/j.ensm.2023.103093.

## References

[1] J. Yu, B.-Q. Li, C.-X. Zhao, Q. Zhang, Seawater electrolyte-based metal-air batteries: from strategies to applications, Energy Environ. Sci. 13 (2020) 3253–3268, https://doi.org/10.1039/d0ee0.1617a.

[2] M. Son, S. Park, N. Kim, A.-T. Angeles, Y. Kim, K.-H. Cho, Simultaneous energy storage and seawater desalination using rechargeable seawater battery: feasibility and future directions, Adv. Sci. 8 (2021), 2101289, https://doi.org/10.1002/advs.202101289.

[3] S. Arnold, L. Wang, V. Presser, Dual-use of seawater batteries for energy storage and water desalination, Small 18 (2022), 2107913, https://doi.org/10.1002/smll.202107913.

[4] S.-M. Hwang, J.-S. Park, Y. Kim, W. Go, J. Han, Y. Kim, Y. Kim, Rechargeable seawater batteries-from concept to applications, Adv. Mater. 31 (2019), 1804936, https://doi.org/10.1002/adma.201804936.

[5] S.-T. Senthilkumar, W. Go, J. Han, L. Pham Thi Thuy, K. Kishor, Y. Kim, Y. Kim, Emergence of rechargeable seawater batteries, J. Mater. Chem. A 7 (2019) 22803–22825, https://doi.org/10.1039/c9ta08321a.

[6] L. Yu, Q. Zhu, S. Song, B. McElhenny, D. Wang, C. Wu, Z. Qin, J. Bao, Y. Yu, S. Chen, Z. Ren, Non-noble metal-nitride based electrocatalysts for high-performance alkaline seawater electrolysis, Nat. Commun. 10 (2019) 5106, https://doi.org/10.1038/s41467-019-13092-7.

[7] M. Yu, X.-Q. Mu, W.-T. Meng, Z.-Y. Chen, Y. Tong, Y. Ge, S.-Y. Pang, S.-J. Li, S.-L. Liu, S.-C. Mu, Tunable atomic-scale steps and cavities break both stability and activity limits of $CoO_x$ nanosheets for catalyzing oxygen evolution, Renewables 1 (2023) 465–473, https://doi.org/10.31635/renewables.023.202300025.

[8] L.-J. Yuan, X.-L. Sui, H. Pan, Z.-B. Wang, Strategies and mechanism for enhancing intrinsic activity of metal-nitrogen-carbon catalysts in electrocatalytic application, Renewables 1 (2023) 514–540, https://doi.org/10.31635/renewables.023.202300023.

[9] J.F. Chang, Y. Yang, Advancements in seawater electrolysis: progressing from fundamental research to practical application, Renewables 1 (2023) 415–454, https://doi.org/10.31635/renewables.0 23.202300034.

[10] J.-K. Kim, E. Lee, H. Kim, C. Johnson, J. Cho, Y. Kim, Rechargeable Seawater Battery and Its Electrochemical Mechanism, ChemElectroChem 2 (2015) 328–332, https://doi.org/10.1002/celc.20.1402344.

[11] Q. Lu, H. Wu, X.-R. Zheng, Y.-H. Cao, J.-H. Li, Y. Wang, H.-Z. Wang, C.-Y. Zhi, Y.-D. Deng, X.-P. Han, W.-B. Hu, Controllable constructing janus homologous heterostructures of transition metal alloys/sulfides for efficient oxygen electrocatalysis, Adv. Energy Mater. 12 (2022), 2202215, https://doi.org/10.1002/aenm.202202215.

[12] X.-R. Zheng, Y.-H. Cao, Z. Wu, W.-L. Ding, T. Xue, J.-J. Wang, Z.-L. Chen, X.-P. Han, Y.-D. Deng, W.-B. Hu, Rational design and spontaneous sulfurization of NiCo-(oxy) Hydroxysulfides nanosheets with modulated local electronic configuration for enhancing oxygen electrocatalysis, Adv. Energy Mater. 12 (2022), 2103275, https://doi.org/10.1002/aenm.202103275.

[13] X. Wan, Q. Liu, J. Liu, S. Liu, X. Liu, L. Zheng, J. Shang, R. Yu, J. Shui, Iron atom-cluster interactions increase activity and improve durability in Fe-N-C fuel cells, Nat. Commun. 13 (2022) 2963, https://doi.org/10.1038/s41467-022-30702-z.

[14] T.-J. Schmidt, U.-A. Paulus, H.-A. Gasteiger, R.-J. Behm, The oxygen reduction reaction on a Pt/carbon fuel cell catalyst in the presence of chloride anions, J. Electroanal. Chem. 508 (2001) 41–47, https://doi.org/10.1016/s0022-0728(01)00499-5.

[15] T.-M. Arruda, B. Shyam, J.-M. Ziegelbauer, S. Mukerjee, D.-E. Ramaker, Investigation into the competitive and site-specific nature of anion adsorption on Pt using in situ X-ray absorption spectroscopy, J. Phys. Chem. C 112 (2008) 18087–18097, https://doi.org/10.1021/jp8067359.

[16] N. Job, M. Chatenet, S. Berthon-Fabry, S. Hermans, F. Maillard, Efficient Pt/carbon electrocatalysts for proton exchange membrane fuel cells: avoid chloride-based Pt salts!, J. Power Sources 240 (2013) 294–305, https://doi.org/10.1016/j.jpowsour.2013.03.188.

[17] Z.-Y. Sun, Y. Ding, C. Wang, P. Mao, B.-B. Wang, R. Ran, W. Zhou, K.-M. Liao, Z.-P. Shao, A magnetic binder-linked air electrode with anti-pulverization behavior for rechargeable and recyclable Zn-air batteries, Adv. Funct. Mater. 33 (2023), 2302234, https://doi.org/10.1002/adfm.202302234.

[18] X.-R. Zheng, Y.-H. Cao, H.-Z. Wang, J.-F. Zhang, M.-H. Zhao, Z. Hang, Y. Wang, L. Zhang, Y.-D. Deng, W.-B. Hu, X.-P. Han, Designing breathing air-electrode and enhancing the oxygen electrocatalysis by thermoelectric effect for efficient Zn-air batteries, Angew. Chem. Int. Ed. 62 (2023), e202302689, https://doi.org/10.1002/anie.202302689.

[19] Q. Zhao, Y. Wang, W.-H. Lai, F. Xiao, Y. Lyu, C. Liao, M. Shao, Approaching a high-rate and sustainable production of hydrogen peroxide: oxygen reduction on Co-N-C single-atom electrocatalysts in simulated seawater, Energy Environ. Sci. 14 (2021) 5444–5456, https://doi.org/10.1039/d1ee00878a.

[20] X. Zhang, T.-P. Lai, X. Liao, V. Papaefthimiou, M. Pugliesi, G. Tuci, G. Giambastiani, S. Pronkin, P.-H. Cuong, Inducing atomically dispersed Cl-$FeN_4$ sites for ORRs in the $SiO_2$-mediated synthesis of highly mesoporous N-enriched C-networks, J. Mater. Chem. A 10 (2022) 6153–6164, https://doi.org/10.1039/d1ta09519f.

[21] S. Kim, S. Ji, H. Yang, H. Son, H. Choi, J. Kang, O.-L. Li, Near surface electric field enhancement: pyridinic-N rich few-layer graphene encapsulating cobalt catalysts as highly active and stable bifunctional ORR/OER catalyst for seawater batteries, Appl. Catal. B 310 (2022), 121361, https://doi.org/10.1016/j.apcatb.2022.121361.

[22] X.-P. Han, X.-F. Ling, Y. Wang, T.-Y. Ma, C. Zhong, W.-B. Hu, Y.-D. Deng, Generation of nanoparticle, atomic-cluster, and single-atom cobalt catalysts from zeolitic imidazole frameworks by spatial isolation and their use in zinc-air batteries, Angew. Chem. Int. Ed. 58 (2019) 5359–5364, https://doi.org/10.1002/anie.201901109.

[23] C. Xia, Y.-R. Qiu, Y. Xia, P. Zhu, G. King, X. Zhang, Z.-Y. Wu, J.-Y. Kim, D.-A. Cullen, D.-X. Zheng, P. Li, M. Shakouri, E. Heredia, P.-X. Cui, H.-N. Alshareef, Y.-F. Hu, H.-T. Wang, General synthesis of single-atom catalysts with high metal loading using graphene quantum dots, Nat. Chem. 13 (2021) 887–894, https://doi.org/10.1038/s41557-021-00734-x.

[24] Y. Wang, X.-P. Li, M.-M. Zhang, J.-F. Zhang, Z.-L. Chen, X.-R. Zheng, Z.-L. Tian, N.-Q. Zhao, X.-P. Han, K. Zaghib, Y.-S. Wang, Y.-D. Deng, W.-B. Hu, Highly Active and durable single-atom tungsten-doped $NiS_{0.5}Se_{0.5}$ nanosheet@$NiS_{0.5}Se_{0.5}$ nanorod heterostructures for water splitting, Adv. Mater. 34 (2022), 2107053, https://doi.org/10.1002/adma.202107053.

[25] C.-Z. Zhu, Q.-R. Shi, B.-Z. Xu, S.-F. Fu, G. Wan, C. Yang, S.-Y. Yao, J.-H. Song, H. Zhou, D. Du, S.-P. Beckman, D. Su, Y.-H. Lin, Hierarchically porous M-N-C (M = Co and Fe) single-atom electrocatalysts with robust $MN_x$ active moieties enable enhanced ORR performance, Adv. Energy Mater. 8 (2018), 1801956, https://doi.org/10.1002/aenm.201801956.

[26] K.-C. Wan, T.-K. Chu, B. Li, P.-W. Ming, C.-M. Zhang, Rational design of atomically dispersed metal site electrocatalysts for oxygen reduction reaction, Adv. Sci. 10 (2023), 2203391, https://doi.org/10.1002/advs.202203391.

[27] X.-H. Xie, C. He, B.-Y. Li, Y.-H. He, D.-A. Cullen, E.-C. Wegener, A.-J. Kropf, U. Martinez, Y.-W. Cheng, M.-H. Engelhard, M.-E. Bowden, M. Song, T. Lemmon, X.-S. Li, Z.-M. Nie, J. Liu, D.-J. Myers, P. Zelenay, G.-F. Wang, G. Wu, V. Ramani, Y.-Y. Shao, Performance enhancement and degradation mechanism identification of a single-atom Co-N-C catalyst for proton exchange membrane fuel cells, Nat. Catal. 3 (2020) 1044–1054, https://doi.org/10.1038/s41929-020-00546-1.

[28] K. Mamtani, D. Jain, A.-C. Co, U.-S. Ozkan, Investigation of chloride poisoning resistance for nitrogen-doped carbon nanostructures as oxygen depolarized cathode catalysts in acidic media, Catal. Lett. 147 (2017) 2903–2909, https://doi.org/10.1007/s10562-017-2205-3.

[29] R. Meng, C. Zhang, Z. Lu, X. Xie, Y. Liu, Q. Tang, H. Li, D. Kong, C.-N. Geng, Y. Jiao, Z. Fan, Q. He, Y. Guo, G. Ling, Q.-H. Yang, An oxygenophilic atomic dispersed Fe-N-C catalyst for lean-oxygen seawater batteries, Adv. Energy Mater. 11 (2021), 2100683, https://doi.org/10.1002/ae nm.202100683.

[30] Q.-Q. Cheng, L.-J. Yang, L.-L. Zou, Z.-Q. Zou, C. Chen, Z. Hu, H. Yang, Single cobalt atom and N codoped Carbon nanofibers as highly durable electrocatalyst for oxygen reduction reaction, ACS Catal. 7 (2017) 6864–6871, https://doi.org/10.1021/acscatal.7b02326.

[31] D. Wang, M.W. Yuan, J.S. Xu, Y.Y. Li, K.F. Shi, H. Yang, H.F. Li, G.B. Sun, Highly active atomically dispersed Co-N-x sites anchored on ultrathin N-doped carbon nanosheets with durability oxygen reduction reaction of zinc-air batteries, ACS Sustain. Chem. Eng. 9 (2021) 16956–16964, https://doi.org/10.1021/acssuschemeng.1c05352.

[32] J.-Y. Qin, H. Liu, P.-C. Zou, R. Zhang, C.-Y. Wang, H.-L. Xin, Altering ligand fields in single-atom sites through second-shell anion modulation boosts the oxygen reduction reaction, J. Am. Chem. Soc. 144 (2022) 2197–2207, https://doi.org/10.1021/jacs.1c11331.

[33] T. Yang, H.-H. Lv, Q.-H. Quan, X.L. Li, H.S. Lu, X.J. Cui, G.B. Liu, L.H. Jiang, Electronic structure modulation of $MoO_2$ via Er-doping for efficient overall water/seawater splitting and Mg/seawater batteries, Appl. Surf. Sci. 615 (2023), 156360, https://doi.org/10.1016/j.apsusc. 2023.156360.

[34] W.-Q. Tang, J.-Y. Tang, K.-M. Liao, Z.-P. Shao, Self-reconstruction of highly active $NiCo_2O_4$ with triple-continuous transfer of electrons, ions, and oxygen for Zn-air batterie, Chem. Eng. J. 455 (2023), 140855, https://doi.org/10.1016/j.cej.2022.140855.

[35] Z.-G. Chen, Y.-F. Xu, D. Ding, G. Song, X.-X. Gan, H. Li, W. Wei, J. Chen, Z.-Y. Li, Z.-M. Gong, X.-M. Dong, C.-F. Zhu, N.-N. Yang, J.-Y. Ma, R. Gao, D. Luo, S. Cong, L. Wang, Z.-G. Zhao, Y. Cui, Thermal migration towards constructing W-W dual-sites for boosted alkaline hydrogen evolution reaction, Nat. Commun. 13 (2022) 763, https://doi.org/10.1038/s41467-022-28413-6.

[36] Y. Wang, X.-P. Li, Z. Huang, H.-Z. Wang, Z.-L. Chen, J.-F. Zhang, X.-R. Zheng, Y.-D. Deng, W.-B. Hu, Amorphous Mo-doped $NiS_{0.5}Se_{0.5}$ Nanosheets@Crystalline $NiS_{0.5}Se_{0.5}$ nanorods for high current-density electrocatalytic water splitting in neutral media, Angew. Chem. Int. Ed. 62 (2023), e202215256. http://doi.org/10.1002/anie.202215256.

[37] M. Liu, J. Lee, T.-C. Yang, F. Zheng, J. Zhao, C.-M. Yang, L.-Y. Lee, Synergies of Fe single atoms and clusters on N-doped carbon electrocatalyst for pH-universal oxygen reduction, Small Methods 5 (2021), 2001165, https://doi.org/10.1002/smtd.202001165.

[38] M. Zhang, H. Li, J. Chen, F.-X. Ma, L. Zhen, Z. Wen, C.-Y. Xu, High-Loading Co single atoms and clusters active sites toward enhanced electrocatalysis of oxygen reduction reaction for high-performance Zn-Air battery, Adv. Funct. Mater. 33 (2022), 2209726, https://doi.org/10.1002/adfm.202209726.

[39] G.-J. Li, J.-P. Liu, C.-L. Xu, H.-D. Chen, H.-A. Hu, R. Jin, L.-T. Sun, H.-F. Chen, C.-Z. Guo, H.-L. Li, Y.-J. Si, Regulating the Fe-spin state by Fe/$Fe_3C$ neighbored single Fe-$N_4$ sites in defective carbon promotes the oxygen reduction activity, Energy Stor. Mater. 56 (2023) 394–402, https://doi.org/10.1016/j.ens m.2023.01.030.

[40] X. Ding, C. Jia, P. Ma, H. Chen, J. Xue, D. Wang, R. Wang, H. Cao, M. Zuo, S. Zhou, Z. Zhang, J. Zeng, J. Bao, Remote synergy between heterogeneous single atoms and clusters for enhanced oxygen evolution, Nano Lett 23 (2023) 3309–3316, https://doi.org/10.1021/acs.nanolett.3c00228.

[41] H. Huang, D. Yu, F. Hu, S.-C. Huang, J. Song, H.-Y. Chen, L.-L. Li, S. Peng, Clusters induced electron redistribution to tune oxygen reduction activity of transition metal single-atom for Metal-Air batteries, Angew. Chem. Int. Ed. 61 (2022), e202116068, https://doi.org/10.1002/anie.202116068.

[42] F. Yu, J. Zhan, D. Chen, J. Guo, S. Zhang, L.-H. Zhang, Electronic states regulation induced by the synergistic effect of Cu clusters and Cu-$S_1N_3$ sites boosting electrocatalytic performance, Adv. Funct. Mater. 33 (2023), 2214425, https://doi.org/10.1002/adfm.202214425.

[43] Q. Lu, H. Wu, X.-R. Zheng, Y.-A. Chen, A.-L. Rogach, X.-P. Han, Y.-D. Deng, W.-B. Hu, Encapsulating cobalt nanoparticles in interconnected N-doped hollow carbon nanofibers with enriched Co-N-C moiety for enhanced oxygen

electrocatalysis in Zn-air batteries, Adv. Sci. 8 (2021), https://doi.org/10.1002/advs.202101438.
[44] M. Newville, IFEFFIT: interactive XAFS analysis and FEFF fitting, J. Synchrotron Radiat. 8 (2001) 322–324, https://doi.org/10.1107/s0909049500016964.
[45] C. Mikutta, R. Kretzschmar, Spectroscopic evidence for ternary complex formation between arsenate and ferric iron complexes of humic substances, Environ. Sci. Technol. 45 (2011) 9550–9557, https://doi.org/10.1021/es202300w.
[46] Y.-Y. Guo, Y.-H. Cao, J.-D. Lu, X.-R. Zheng, Y.-D. Deng, The concept, structure, and progress of seawater metal-air batteries, Microstucture 3 (2023), 2023038, https://doi.org/10.2051/microstruc tures.2023.30.
[47] M.-D. Segall, P.-J. Lindan, M.-J. Probert, C.-J. Pickard, P.-J. Hasnip, S.-J. Clark, M.-C. Payne, First-principles simulation: ideas, illustrations and the CASTEP code, J. Phys. Condens. Matter. 14 (2002) 2717–2744, https://doi.org/10.1088/0953-8984/14/11/301.
[48] J.-P. Perdew, K. Burke, M. Ernzerhof, Generalized gradient approximation made simple, Phys. Rev. Lett. 77 (1996) 3865–3868, https://doi.org/10.1103/PhysRevLett.77.3865.
[49] D.-R. Hamann, M. Schlüter, C. Chiang, Norm-Conserving Pseudopotentials, Phys. Rev. Lett. 43 (1979) 1494–1497, https://doi.org/10.1103/PhysRevLett.43.1494.
[50] S. Grimme, Semiempirical GGA-type density functional constructed with a long-range dispersion correction, J. Comput. Chem. 27 (2006) 1787–1799, https://doi.org/10.1002/jcc.20495.
[51] S.-K. Singh, K. Takeyasu, J. Nakamura, Active sites and mechanism of oxygen reduction reaction electrocatalysis on nitrogen-doped carbon materials, Adv. Mater. 31 (2019), https://doi.org/10.1002/adma.201804297.
[52] Y. Wu, C. Li, W. Liu, H.-H. Li, Y.-Y. Gong, L.-Y. Niu, X.-J. Liu, C.-Q. Sun, S.-Q. Xu, Unexpected monoatomic catalytic-host synergetic OER/ORR by graphitic carbon nitride: density functional theory, Nanoscale 11 (2019) 5064–5071, https://doi.org/10.1039/c8nr09300h.
[53] I. Arcon, A. Tuel, A. Kodre, G. Martin, A. Barbier, EXAFS determination of the size of Co clusters on silica, J. Synchrotron Rad. 8 (2001) 575–577, https://doi.org/10.1107/S0909049500019294.
[54] X.-R. Zheng, Z.-R. Xu, S.-F. Li, Y.-X. Zhang, J.-F. Zhang, C.-G. Kuai, L. Tao, M.-M. Rahman, Y. Zhang, S.-J. Lee, C.-J. Sun, L.-X. Li, W.-B. Hu, D. Nordlund, J. Liu, Y.-J. Liu, F. Lin, Reversible Mn/Cr dual redox in cation-disordered Li-excess cathode materials for stable lithium ion batteries, Acta Mater. 212 (2021), 116935, https://doi.org/10.1016/j.actamat.2021.116935.
[55] Z.-G. Chen, W.-B. Gong, J. Wang, S. Hou, G. Yang, C.-F. Zhu, X.-Y. Fan, Y.-F. Li, R. Gao, Y. Cui, Metallic W/$WO_2$ solid-acid catalyst boosts hydrogen evolution reaction in alkaline electrolyte, Nat. Commun. 14 (2023) 5363, https://doi.org/10.1038/s41467-023-41097-w.
[56] Z.-G. Chen, H.-M. Hu, L.-C. Yin, Z.-G. Zhao, G.Liu J.-H.Choi, F.-X. Geng, Composite non-noble system with bridging oxygen for catalyzing Tafel-type alkaline hydrogen evolution, Proc. Natl. Acad. Sci. U.S.A. 120 (2023), e2209760120, https://doi.org/10.1073/pnas.2209760120.
[57] X.-R. Zheng, X.-P. Han, Y.-H. Cao, Y. Zhang, D. Nordlund, J.-H. Wang, S.-L. Chou, H. Liu, L.-L. Li, C. Zhong, Y.-D. Deng, W.-B. Hu, Identifying dense $NiSe_2$/$CoSe_2$ heterointerfaces coupled with surface high-valence bimetallic sites for synergistically enhanced oxygen electrocatalysis, Adv. Mater. 32 (2020), 2000607, https://doi.org/10.1002/adma.202000607.
[58] T.-Z. Wang, L.-C. Miao, S.-Y. Zheng, H.-Y. Qin, X.-J. Cao, L. Yang, L.-F. Jiao, Interfacial engineering of $Ni_3N$/$Mo_2N$ heterojunctions for urea-assisted hydrogen evolution reaction, ACS Catal. 13 (2023) 4091–4100, https://doi.org/10.1021/acscatal.3c00113.
[59] H. Wu, Q. Lu, Y.-J. Li, M.-H. Zhao, J.-J. Wang, Y.-B. Li, J.-F. Zhang, X.-R. Zheng, X.-P. Han, N.-Q. Zhao, J.-J. Li, Y.-H. Liu, Y.-D. Deng, W.-B. Hu, Structural framework-guided universal design of high-entropy compounds for efficient energy catalysis, J. Am. Chem. Soc. 145 (2023) 1924–1935, https://doi.org/10.1021/jacs.2c12295.